Nano Energy 22 (2016) 475–482

Contents lists available at ScienceDirect

Nano Energy

journal homepage: www.elsevier.com/locate/nanoen

Full paper

Self-standing porous $LiMn_2O_4$ nanowall arrays as promising cathodes for advanced 3D microbatteries and flexible lithium-ion batteries

Hui Xia [a,b,*], Qiuying Xia [a,b], Binghui Lin [a,b], Junwu Zhu [c,**], Joon Kyo Seo [d], Ying Shirley Meng [d,***]

[a] School of Materials Science and Engineering, Nanjing University of Science and Technology, Nanjing 210094, China
[b] HerbertGleiter Institute of Nanoscience, Nanjing University of Science and Technology, Nanjing 210094, China
[c] Key Laboratory of Soft Chemistry and Functional Materials, Nanjing University of Science and Technology, Ministry of Education, Nanjing 210094, China
[d] Department of NanoEngineering, University of California San Diego, La Jolla, CA 92093, USA

ARTICLE INFO

Article history:
Received 22 September 2015
Received in revised form
26 November 2015
Accepted 26 January 2016
Available online 1 February 2016

Keywords:
3D microbatteries
Flexible lithium-ion batteries
Cathode
Self-standing
Porous

ABSTRACT

Three-dimensional self-supported cathode nanoarchitectures are the key to develop high-performance thin film lithium-ion microbatteries and flexible lithium-ion batteries. In this work, we have developed a facile "hydrothermal lithiation" strategy to prepare vertically aligned porous $LiMn_2O_4$ nanowall arrays, comprising highly crystallized spinel nanoparticles, on various conductive substrates without high temperature treatment. The "hydrothermal lithiation" can effectively convert Mn_3O_4 spinel nanowall arrays into $LiMn_2O_4$ spinel nanowall arrays without severe morphology change. The binder-free three-dimensional porous $LiMn_2O_4$ nanowall arrays exhibit high specific reversible capacity up to 131 mA h g^{-1} (or 0.29 mA h cm^{-2}) as well as outstanding cycling stability and rate capability, making them promising as cathodes for both three-dimensional thin film lithium-ion microbatteries and flexible lithium-ion batteries. A flexible lithium-ion full cell is demonstrated by using $LiMn_2O_4$ nanowall arrays on carbon cloth as the cathode and $Li_4Ti_5O_{12}$ nanowall arrays on carbon cloth as the anode. The flexible $Li_4Ti_5O_{12}$//$LiMn_2O_4$ full cell device, employing three-dimensional nanoarchitectures for both cathode and anode, can deliver specific reversible capacities of 124.8 mA h g^{-1} (based on the weight of cathode material) at 1 C and 92.1 mA h g^{-1} at 20 C with excellent cycle performance. Our work demonstrates the great potential for flexible energy storage technology using low cost fabrication method of nanoarchitectures.

1. Introduction

With fast development of microelectronic devices and flexible electronic devices, two emerging battery technologies of thin-film lithium-ion microbatteries and flexible lithium-ion batteries have attracted remarkable attention due to the potential enormous market in the future [1–3]. While the microelectronic industry is developing at a rapid pace with smaller and smaller devices, the implementation of microelectro-mechanical systems (MEMS) on the market heavily depends on the availability of on-board power sources. However, traditional rechargeable batteries based on liquid electrolyte are not applicable due to the restrictions for on-chip design, size, and inherent risk of leakage, which give rise to the development of all-solid-state thin film lithium-ion microbattery technology [4,5]. As more energy is required in microelectronic devices, two-dimensional (2D) thin film microbatteries are no longer the ideal battery design because the limited footprint area results in a compromise between energy density and power density for the built-in power source. A move to all-solid-state three-dimensional (3D) architectures has been proposed as a promising approach to tackle this challenge and achieve both high energy and power densities within the footprint area [6,7]. In the mean time, the flexible electronics is emerging as a successful technology for the next generation flexible optoelectronic devices in various applications such as rollup displays, smart electronics, and wearable devices, which find flexible lithium-ion batteries as the reliable power supply [8]. Flexible lithium-ion batteries adopt the same core battery components and working principles with the conventional lithium-ion batteries, but require high flexibility

* Corresponding author at: School of Materials Science and Engineering, Nanjing University of Science and Technology, Nanjing 210094, China.
** Corresponding author.
*** Corresponding author.
E-mail addresses: xiahui@njust.edu.cn (H. Xia), zhujw@njust.edu.cn (J. Zhu), shmeng@ucsd.edu (Y.S. Meng).

http://dx.doi.org/10.1016/j.nanoen.2016.01.022

and mechanical strength for both anode and cathode [9–11].

3D microbatteries generally require the fabrication of 3D nanoarchitectured electrodes with large capacity at high charge/discharge rates and long-term cycling capability [12]. Without using binders or conductive additives, the direct fabrication of nanoarchitectures for the electrode materials on conductive substrates represents a new class of electrodes: 3D self-supported electrodes [13,14]. Except for the key component for constructing 3D microbatteries, the 3D self-supported electrodes using flexible substrates, such as metal foil and carbon cloth, can be ideal electrodes for flexible lithium-ion batteries [15–17]. Active research efforts have been made to the synthesis and characterization of various 3D self-supported electrodes on different conductive substrates [18,19]. Most of the previous works, however, focused on the preparation of 3D self-supported nanoarchitectures for anode materials such as Si [20], Co_3O_4 [21], and TiO_2 [22,23], while very limited work has been reported on the 3D self-supported nanoarchitectures for cathode materials [24,25]. The difficulty lies in the fact that the synthesis of cathode materials such as $LiCoO_2$ and $LiMn_2O_4$ involves high temperature treatment, which is hard to retain the nanostructures after heat treatment. Moreover, the flexible substrate such as carbon cloth is not stable at temperature above 400 °C in the air, which makes the fabrication of flexible cathode a great challenge. As lithium source in lithium-ion batteries, cathode plays a pivotal role in determining the electrochemical performance of microbatteries and flexible lithium-ion batteries. Therefore, fabrication of high quality 3D self-supported cathode nanoarchitectures will be the key to accomplish the construction of 3D microbatteries and flexible lithium-ion batteries and further boost their energy density and power density.

$LiMn_2O_4$ is one of the most attractive cathode materials for lithium-ion batteries owing to its low cost, environmentally friendliness, high electrochemical performance, and simple synthesis. Various $LiMn_2O_4$ nanostructures, including nanowires [26], nanotubes [27], and nanoparticles [28], have been reported, showing improved electrochemical performances compared to bulk $LiMn_2O_4$ powders. However, these $LiMn_2O_4$ nanostructures are not applicable to microbatteries or flexible lithium-ion batteries without the support of conductive substrates and self-standing feature. By far, there are only a couple of trials that have been reported to fabricate 3D self-supported $LiMn_2O_4$ nanoarchitectures. Early works by Park and Bettge reported the fabrication of 3D porous $LiMn_2O_4$ thin films [29] and textured $LiMn_2O_4$ thin films [30] by using templates and magnetron sputtering technique, however the obtained 3D $LiMn_2O_4$ thin films showed low specific capacitance per area due to the low mass loading, without mentioning the high fabrication cost and tedious fabrication procedure. Shen et al. prepared carbon fiber loaded $LiMn_2O_4$ nanoparticles for flexible batteries by adopting a conversion from MnO_2 to $LiMn_2O_4$, but could not control the morphology change during the conversion [32]. The original morphology of MnO_2 cannot be retained after the conversion, which is probably due to the significant structural difference between MnO_2 and $LiMn_2O_4$. Therefore, a facile and scalable fabrication strategy is imperative to prepare the 3D self-supported $LiMn_2O_4$ nanoarchitectures to apply in 3D microbatteries and flexible lithium-ion batteries. In this work, we developed a novel one-step "hydrothermal lithiation" method to prepare 3D porous $LiMn_2O_4$ nanowall arrays on both metal and carbon substrates at low temperature. The self-standing $LiMn_2O_4$ nanostructures were constructed by using Mn_3O_4 nanostructure as the template with a tender spinel-to-spinel conversion route from Mn_3O_4 to $LiMn_2O_4$. The 3D porous $LiMn_2O_4$ nanowall arrays exhibited large reversible specific capacity as well as outstanding cycling stability and rate capability, making them promising as cathodes for 3D microbatteries and flexible lithium-ion batteries. For demonstration purpose, a flexible lithium-ion full cell in pouch format, coupling the $LiMn_2O_4$ nanowall arrays as cathode and the $Li_4Ti_5O_{12}$ nanowall arrays as anode, was successfully fabricated, delivering promising electrochemical performance. To the best of our knowledge, this work will be the first report introducing the fabrication of vertically aligned $LiMn_2O_4$ nanowall arrays on various substrates by a solution method at low temperature.

2. Experimental section

2.1. Preparation of 3D self-supported $LiMn_2O_4$ nanowall arrays

The 3D self-supported porous $LiMn_2O_4$ nanowall arrays were fabricated using a one-step hydrothermal treatment to achieve the chemical lithiation to the porous Mn_3O_4 nanowall arrays and the synthesis procedure is illustrated in Fig. 1a. The porous Mn_3O_4 nanowall arrays were deposited on the Au (or carbon cloth) substrates by cathodic deposition according to our previous work [31]. For the cathodic deposition, a three-electrode electrochemical cell was used with a solution of 0.015 M manganese acetate (99%, Aldrich) and 0.015 M sodium sulfate (99%, Aldrich) as the electrolyte. The electrochemical cell consists of a Au foil (1 cm^2, or carbon cloth, about 4 cm^2) as the working electrode, a platinum foil (about 4 cm^2) as the counter electrode, and a Ag/AgCl (in saturated KCl) as the reference electrode. The cathodic depositions were carried out on both Au and carbon cloth substrates at a constant potential of −1.4 V vs. Ag/AgCl for 900 s. After deposition, the Au (or carbon cloth) supported $Mn(OH)_2$ was cleaned with distilled water and dried in the air at room temperature overnight to convert into Mn_3O_4. The Au substrate supported Mn_3O_4 nanowall arrays were immersed into a 15 mL 0.02 M LiOH solution, which was then transferred into a 50 mL Teflon-lined stainless steel autoclave and heated at three different temperatures (200, 220, and 240 °C) for 17 h. After cooling down to room temperature, the obtained $LiMn_2O_4$ nanowall arrays were rinsed with distilled water and dried in oven at 100 °C in the air for further characterization. To construct the full cell device, $Li_4Ti_5O_{12}$ nanowall arrays were grown on the carbon cloth by a similar hydrothermal synthesis according to the literature [32].

2.2. Materials characterization

The crystallographic information and phase purity of the samples were characterized by X-ray powder diffraction (XRD, Bruker-AXS D8 Advance), Raman spectroscopy (Jobin-Yvon T6400 Micro-Raman system), and X-ray photoelectron spectroscopy (Phi Quantera SXM spectrometer using Al Kα X-ray as the excitation source). The morphology and microstructure of the samples were investigated by field emission scanning electron microscopy (FESEM, Hitachi S4300), transmission electron microscopy (TEM), and high-resolution transmission electron microscopy (HRTEM, FEI Tecnai 20).

2.3. Electrochemical measurements

The Au or carbon cloth substrates supported $LiMn_2O_4$ nanowall arrays without any binders or conductive additives were directly used as the cathodes. Half cells using lithium foils as both counter and reference electrodes were assembled with Swagelok cells in the glove box for electrochemical measurement. For all electrochemical measurements, 1 M $LiPF_6$ in ethylene carbonate and diethyl carbonate (v/v=1:1) solution was used as the electrolyte and Celgard 2400 was used as the separator. Cyclic voltammetry (CV) measurements were carried out in the voltage range between 3 and 4.4 V (vs. Li/Li^+) at various scan rates from 0.1 to 10 mV s^{-1}

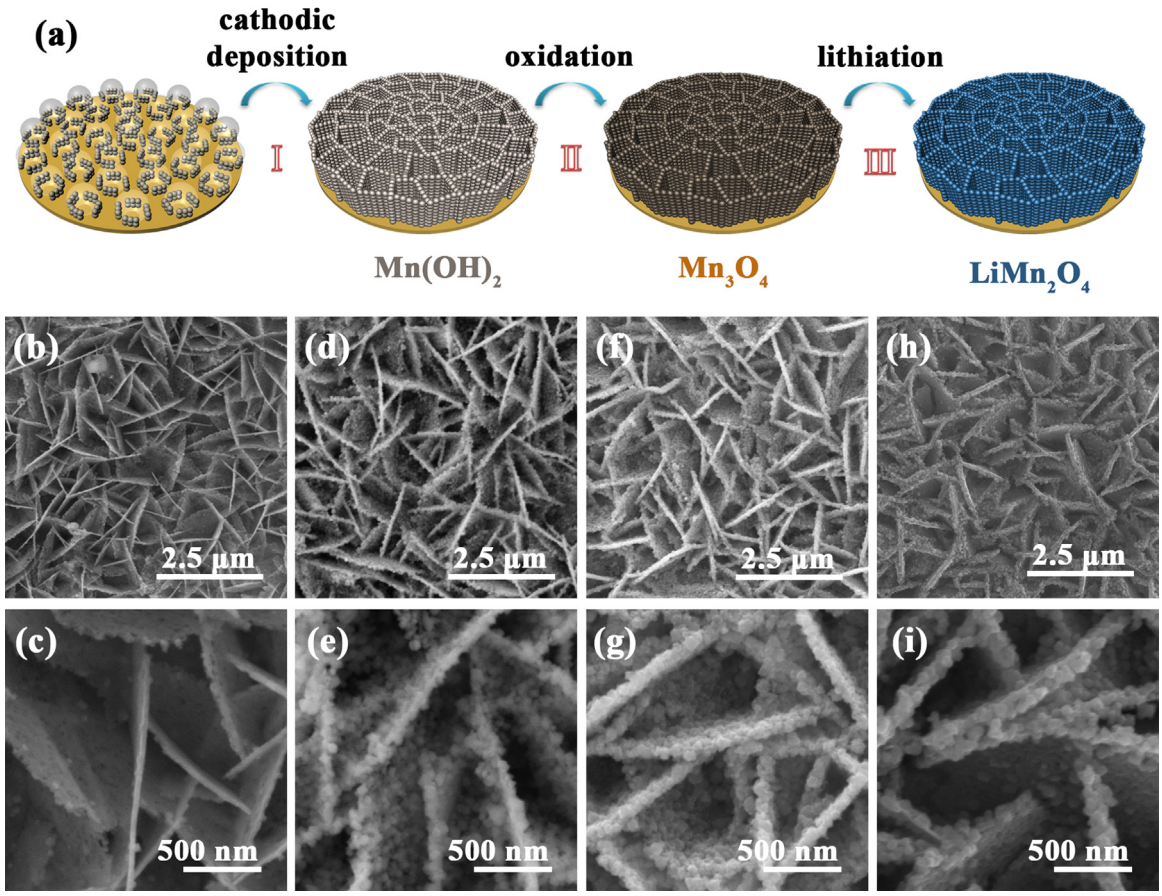

Fig. 1. (a) Schematic illustration of fabrication procedure of the 3D porous $LiMn_2O_4$ nanowall arrays on Au substrate. FESEM images of the as-prepared Mn_3O_4 nanowall arrays (b and c), 200 °C synthesized $LiMn_2O_4$ nanowall arrays (d and e), 220 °C synthesized $LiMn_2O_4$ nanowall arrays (f and g), and 240 °C synthesized $LiMn_2O_4$ nanowall arrays (h and i).

using CHI660D electrochemical workstation. Galvanostatic charge/discharge measurements were carried out in the voltage range between 3 and 4.4 V at different C rates (1 C = 148 mA h g^{-1}) using LAND CT2001A battery tester. To construct the flexible lithium-ion full cell, the carbon cloth substrate supported $Li_4Ti_5O_{12}$ nanowall arrays were used as the anode to couple with the $LiMn_2O_4$ cathode and sealed inside an Al/polyethylene film. The mass ratio of $LiMn_2O_4/Li_4Ti_5O_{12}$ was set to be 0.86 for the full cell to attain matched capacities for cathode and anode. The full cell was charged and discharged between 1.6 and 3 V at different C rates (1 C = 148 mA h g^{-1}). The calculation of the specific capacities for both half cells and full cells were based on the mass of $LiMn_2O_4$. The mass loadings of active materials on different substrates were measured by a Sartorius Analytical balance (CPA225D, with a resolution of 10 μg) and were estimated in the range between 1 and 2 mg cm^{-2}. For the carbon cloth supported $LiMn_2O_4$ nanowall arrays, the mass ratio between the active material (~2 mg cm^{-2}) and the carbon cloth (~10 mg cm^{-2}) is about 1:5. The active material loading of the present work (1~2 mg cm^{-2}) is comparable to that of literature reports on loading active material on the carbon textile for flexible lithium-ion batteries [11,17].

3. Results and discussion

As high-temperature treatment is usually detrimental to fabrication of nanostructures for cathode materials, we developed a low-temperature "hydrothermal lithiation" method to fabricate 3D porous $LiMn_2O_4$ nanowall arrays on different conductive substrates. As illustrated in Fig. 1a, the "hydrothermal lithiation" can enable the chemical lithiation to the preformed Mn_3O_4 nanowall arrays and convert them to $LiMn_2O_4$ nanowall arrays without altering the 3D nanoarchitecture. The 3D porous Mn_3O_4 nanowall arrays were prepared by a cathodic deposition method utilizing H_2 bubbles as the template. As the reduction potential of Mn^{2+} to Mn ($E^\circ = -1.180$ V vs. normal hydrogen electrode (NHE) at 25 °C) is much more negative than that of water electrolysis ($E^\circ = -0.828$ V vs. NHE at 25 °C), the H_2 evolution is preferred to occur at the working electrode when applying a negative potential of −1.4 V vs. Ag/AgCl [33]. At the same time, the water electrolysis generates a high OH^- concentration near the cathode, which enables $Mn(OH)_2$ precipitation at the working electrode. In the cathodic deposition process, the H_2 bubbles which were formed continuously at the working electrode function as dynamic template, forming the 3D porous nanoarchitecture for $Mn(OH)_2$. Since $Mn(OH)_2$ is not stable in the presence of oxygen, it is readily oxidized to Mn_3O_4 after drying in the air, while remaining the same morphology. In the final stage, the "hydrothermal lithiation" can insert lithium into Mn_3O_4 effectively to develop $LiMn_2O_4$ without changing the morphology, providing a facile method to fabricate 3D nanoarchitectures for the $LiMn_2O_4$ cathode materials. From the optical images of the different films on Au substrates (Supporting information, Fig. S1), it is clear to see the color change from transparent to yellow and from yellow to black, corresponding to the phase transitions from $Mn(OH)_2$ to Mn_3O_4 and Mn_3O_4 to $LiMn_2O_4$.

Fig. 1b–i shows the surface morphologies of the as-prepared Mn_3O_4 nanowall arrays and the $LiMn_2O_4$ nanowall arrays

synthesized at three different hydrothermal temperatures of 200, 220, and 240 °C on the Au substrates. As shown in Fig. 1b and c, the Mn_3O_4 film prepared by cathodic deposition is composed of nearly vertically aligned 2D nanowalls of about 2 μm in lateral length with similar size micropores in between. The enlarged FESEM image in Fig. 1c demonstrates that every nanowall is composed of interconnected nanocrystallines. The formation of the macroporous nanowall arrays can be understood by the cathodic deposition process. During the cathodic deposition, water electrolysis generates H_2 bubbles at the cathode surface and increases the OH^- concentration in the vicinity of cathode surface. The continuous generation of H_2 bubbles at the cathode surface functions as dynamic template, which prevents uniform precipitation on the substrate [34]. The precipitation can only take place at the free space between H_2 bubbles, thus forming the hierarchical nanowall arrays by continuously stacking the nanoparticles. After the "hydrothermal lithiation," the morphology of the macroporous nanowall arrays was well preserved and was not influenced by the hydrothermal temperature. As the hydrothermal temperature increases, the nanowall thickness increases with larger particle size, indicating the lithiation to the Mn_3O_4 nanowalls and grain growth at higher temperatures.

As illustrated in Fig. 2a, the tetrahedral Mn_3O_4 (hausmannite, space group $I4_1/amd$), which can be expressed as $Mn^{2+}(Mn^{3+})_2O_4$, is a normal spinel with Mn^{2+} and Mn^{3+} ions occupying the tetrahedral and octahedral sites, respectively. Similar to Mn_3O_4, $LiMn_2O_4$ also adopts a spinel structure (space group Fd-$3m$) but with Li^+ staying in the tetrahedral sites and all Mn^{3+}/Mn^{4+} staying in the octahedral sites. During the "hydrothermal lithiation," Mn_3O_4 could react with LiOH and dissolved O_2 in the solution to form $LiMn_2O_4$ phase according to the following reaction:

$$8Mn_3O_4+12LiOH+5O_2\rightarrow 12LiMn_2O_4+6H_2O \quad (1)$$

When Mn^{2+} is oxidized to higher oxidation states, the Mn^{3+} or Mn^{4+} may not be stable in the tetrahedral sites and move to octahedral sites, leaving the tetrahedral sites occupied by the inserted Li^+. The possible conversion mechanism from Mn_3O_4 to $LiMn_2O_4$ during "hydrothermal lithiation" is illustrated in Fig. S2 (Supporting information). The phase evolution was investigated by XRD and Raman Spectroscopy. Fig. 2b shows the XRD patterns of the pristine Mn_3O_4 nanowall arrays and $LiMn_2O_4$ nanowall arrays at three different hydrothermal temperatures of 200, 220, and 240 °C on the Au substrates. Besides the diffraction peaks from the Au substrate, all other diffraction peaks can be indexed to the tetrahedral hausmannite Mn_3O_4 (JCPDS No. 24-0734). After hydrothermal treatment at 200 °C, most diffraction peaks of Mn_3O_4 disappeared, while a new peak emerged as a shoulder to the (101) peak of Mn_3O_4, indicating the existence of two phases in the sample. The new peak can be attributed to the (111) reflection of the spinel $LiMn_2O_4$ (JCPDS No. 35-0782), revealing that certain portion of Mn_3O_4 was converted to $LiMn_2O_4$. When the hydrothermal temperature was increased to 220 °C, no more diffraction peaks from Mn_3O_4 was observed, suggesting the conversion was completed. When the temperature was further increased to 240 °C, the (111) peak for the $LiMn_2O_4$ became very sharp, indicating the successful fabrication of the $LiMn_2O_4$ nanowall arrays with a high degree of crystallinity. According to the (111) peak position of the 240 °C synthesized sample, the c-lattice constant of the 3D $LiMn_2O_4$ nanowall arrays is calculated to be 8.239 Å, which is slightly smaller than the value of stoichiometric $LiMn_2O_4$ (8.248 Å, JCPDS no. 35-0782) reported in

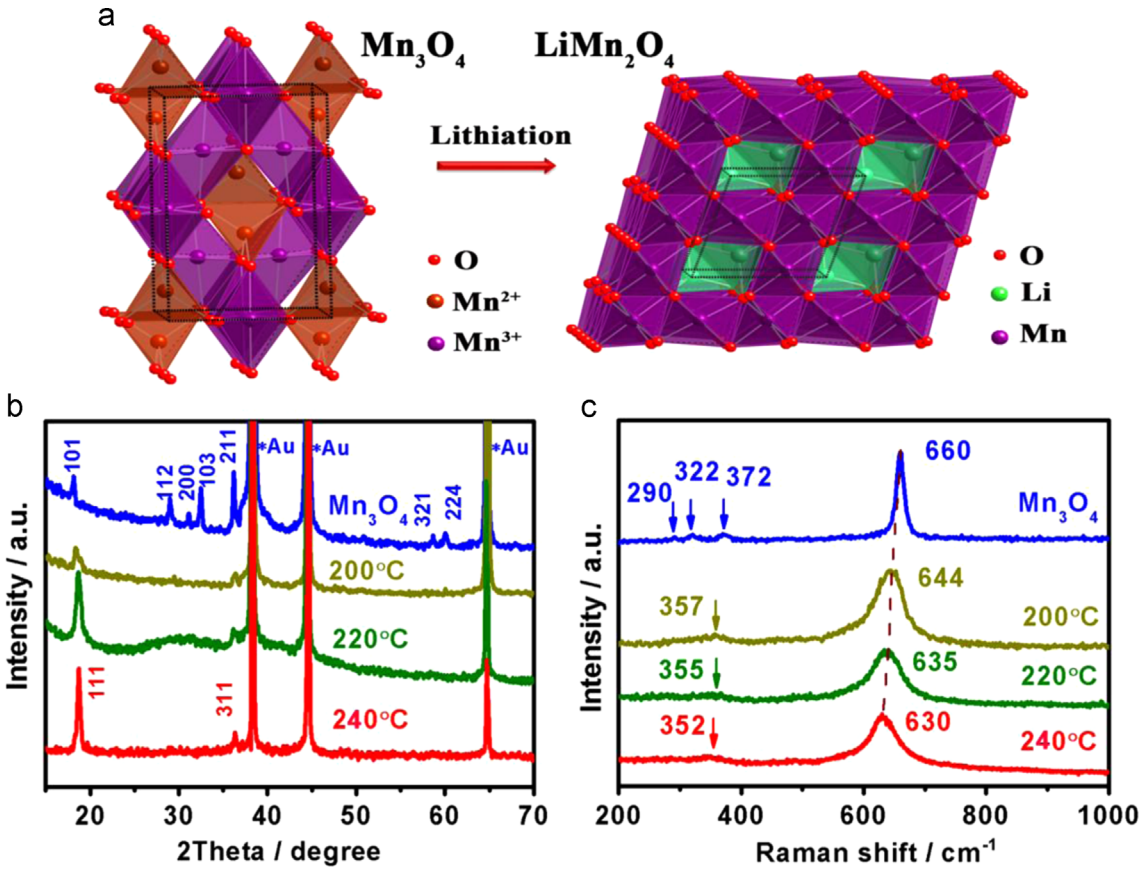

Fig. 2. (a) Crystal structures of spinel Mn_3O_4 and spinel $LiMn_2O_4$. (b) XRD patterns of the Mn_3O_4 nanowall arrays and $LiMn_2O_4$ nanowall arrays synthesized at different temperatures on the Au substrates. (c) Raman spectra of the Mn_3O_4 nanowall arrays and $LiMn_2O_4$ nanowall arrays synthesized at different temperatures on the Au substrates.

the literature [40], showing Li excess in the hydrothermally prepared spinel samples. As 240 °C is the temperature limit for our hydrothermal system, further increasing the temperature could cause safety issues. The structural evolution of the samples synthesized at 240 °C with various synthesis times from 1 to 24 h was characterized by XRD (Supporting Information, Fig. S3). All XRD patterns of the $LiMn_2O_4$ nanowall arrays show no diffraction peaks from Mn_3O_4, suggesting the conversion from Mn_3O_4 to $LiMn_2O_4$ is fast and complete.The intensity of diffraction peaks from $LiMn_2O_4$ builds up as the synthesis time lasts up to 17 h, indicating the degree of crystallinity of $LiMn_2O_4$ can be improved with longer synthesis time. After 17 h, further increasing the synthesis time is not necessary as the XRD pattern of 24 h is similar to that of 17 h, implying 17 h synthesis time is enough to achieve a high degree of crystallinity for the sample. Raman measurements were further carried out to provide complementary structural information to diffraction. Fig. 2c shows the Raman spectra of the pristine Mn_3O_4 nanowall arrays and the $LiMn_2O_4$ nanowall arrays at three different hydrothermal temperatures of 200, 220, and 240 °C on the Au substrates. The Raman spectrum of the Mn_3O_4 nanowall arrays shows a strong peak at 660 cm^{-1}, which is the characteristic peak for Mn_3O_4 spinel, corresponding to the Mn–O breathing vibration of Mn^{2+} ions in tetrahedral coordination (A_{1g} mode) [35,36]. Other small peaks at 290, 322, and 372 cm^{-1} can be attributed to the $T_{2g}(1)$, E_g, and $T_{2g}(2)$ modes of Mn_3O_4, respectively. After hydrothermal treatment, it can be seen that the A_{1g} peak shifted to lower energies with increasing hydrothermal temperature. As discussed by Julien et al. [37], the A_{1g} mode correlated with Mn–O vibration of MnO_6 groups will shift to lower energies as the average Mn oxidation state increases. Moreover, the peak energy decreases with the decrease of trigonal distortion represented by the c/a ratio from 1.64 of Mn_3O_4 to 1.00 of $LiMn_2O_4$. For the 240 °C prepared sample, the Raman spectrum shows the A_{1g} mode at 630 cm^{-1}, agreeing well with the literature report for the $LiMn_2O_4$ spinel [38]. XPS core-level spectra of Mn 2p and Mn 3p of the Mn_3O_4 nanowall arrays before and after lithiation clearly display the emergence of Li signal and oxidation of Mn to higher oxidation states after lithiation (Supporting Information, Fig. S4), further validating the phase transition from Mn_3O_4 to $LiMn_2O_4$ during "hydrothermal lithiation".

The above morphology and structural characterization indicates the 3D self-standing $LiMn_2O_4$ nanowall arrays can be successfully prepared by the "hydrothermal lithiation" method. To validate this approach is applicable to different substrates, carbon cloth was used as the substrate to prepare the 3D $LiMn_2O_4$ cathode, which could be used in flexible batteries. The XRD results show similar phase transition from Mn_3O_4 to $LiMn_2O_4$ on the

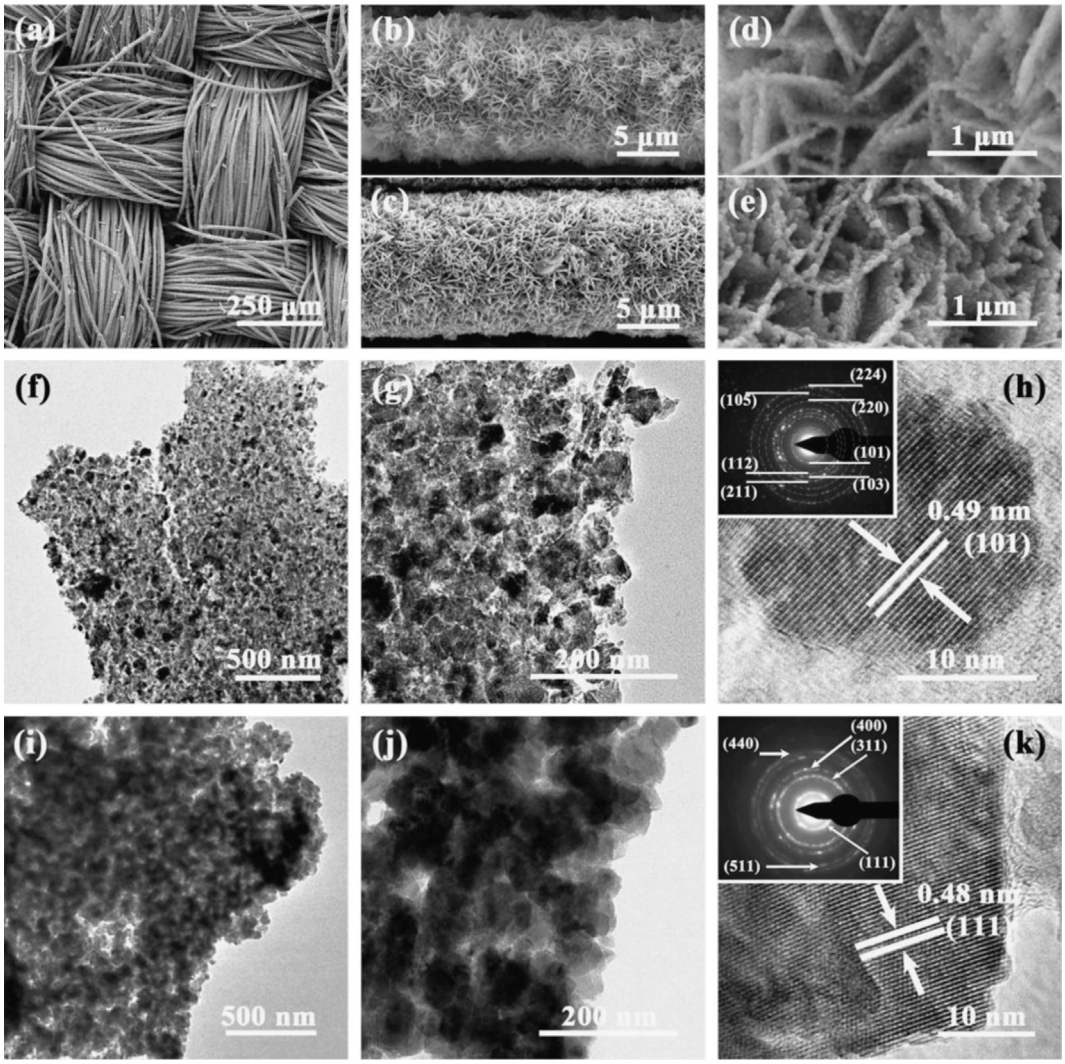

Fig. 3. (a) FESEM image of $LiMn_2O_4$ nanowall arrays grown on the carbon cloth. (b and c) FESEM images of Mn_3O_4 nanowall arrays grown on the single carbon fiber with different magnifications. (d and e). FESEM images of $LiMn_2O_4$nanowall arrays grown on the single carbon fiber with different magnifications.TEM images of Mn_3O_4 nanowalls with different magnifications (f–h).TEM images of $LiMn_2O_4$ nanowalls with different magnifications (i–k). Inset in h is the SEAD pattern for Mn_3O_4 nanowalls. Inset in k is the SEAD pattern for $LiMn_2O_4$ nanowalls.

carbon cloth substrate (Supporting Information, Fig. S5). Fig. 3a shows a low-magnification FESEM image of the prepared $LiMn_2O_4$ nanowall arrays grown on the carbon cloth, demonstrating a uniform coating on the ordered woven structure. Fig. 3b and c illustrate the FESEM images of the Mn_3O_4 and $LiMn_2O_4$ nanowall arrays grown on the single carbon fiber, respectively, exhibiting a core–shell structure. The enlarged FESEM images in Fig. 3d and e show the porous shell on the carbon fiber is composed of cross-linked nanowalls of 20 to 50 nm in thickness, which is similar to the film morphology on the Au substrate. Fig. 3f and g display the TEM images of one Mn_3O_4 nanowall with low and high magnifications, respectively, presenting a mesoporous structure. The nanowall is composed of numerous interconnected nanocrystallines of 10 to 40 nm in size. The HRTEM image of a single Mn_3O_4 particle (Fig. 3h) shows well-defined lattice fringes with an interplanar spacing of 4.9 nm, corresponding to the (101) planes of the tetrahedral Mn_3O_4. The SEAD pattern obtained from the mesoporous nanowall (Inset in Fig. 3h) indicates a polycrystalline structure, and all diffraction rings can be well indexed to the Mn_3O_4 spinel. The dark nanowall image in Fig. 3i displays a larger nanowall thickness for $LiMn_2O_4$, implying the volume expansion from Mn_3O_4 to $LiMn_2O_4$. Along with increased wall thickness, the particle size also increased in the range between 40 and 80 nm after the "hydrothermal lithiation," agreeing well with the FESEM results. The HRTEM image of a single $LiMn_2O_4$ particle (Fig. 3k) proves well-defined lattice fringes with an interplanar spacing of 4.8 nm, corresponding to the (111) planes of the cubic $LiMn_2O_4$. The SEAD pattern (Inset in Fig. 3k) and HRTEM further confirm the formation of highly crystalline $LiMn_2O_4$ nanowalls by the low-temperature synthesis. TEM images of the 200, 220, and 240 °C synthesized samples are compared in Fig. S6 (Supporting Information), demonstrating the crystal growth and improvement in crystallinity at high synthesis temperatures. MnO_2 nanowall arrays were also used in similar hydrothermal condition to produce $LiMn_2O_4$ by Liu et al. [39]. However, the nanowall morphology cannot be retained after lithiation and the nanowall becomes large particles pile up on the substrate. It is speculated that both the initial microstructure and crystal structure of manganese oxide are critical to the final morphology of $LiMn_2O_4$ after lilthiation. In the present work, the Mn_3O_4 nanowalls possess a mesoporous structure, which not only facilitates lithiation over larger surface area but also provides improved structural stability during the phase transition. The numerous pores in the nanowalls can accommodate larger volume change or stain during the lithiation, thus retaining the primary nanowall morphology. Moreover, due to the structural similarity between Mn_3O_4 and $LiMn_2O_4$, the phase transition may proceed more smoothly with less morphological change compared to the phase transition from MnO_2 to $LiMn_2O_4$.

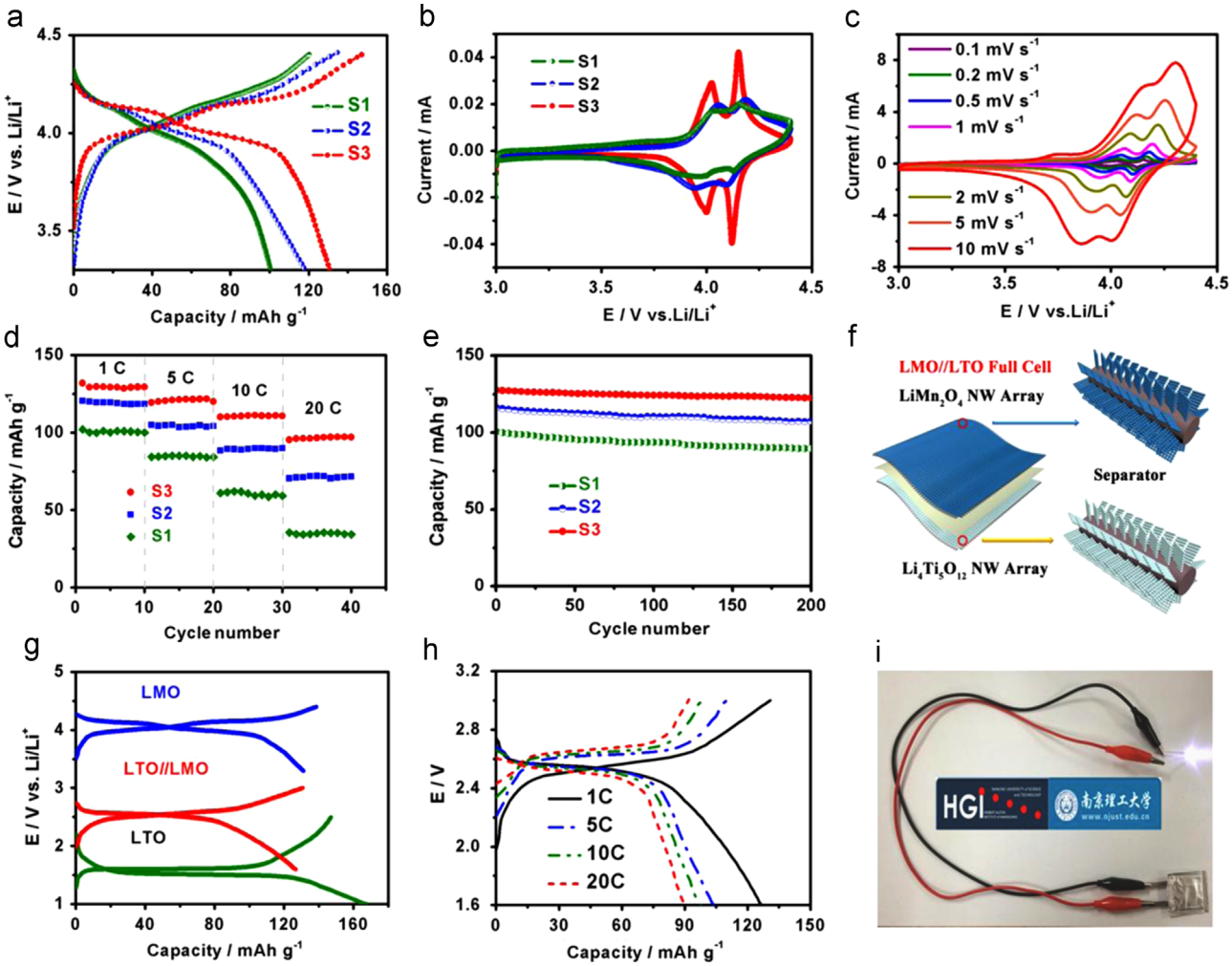

Fig. 4. (a) The first charge/discharge curves of $LiMn_2O_4$ nanowall arrays synthesized at different temperatures. (b) Typical CV curves of $LiMn_2O_4$ nanowall arrays synthesized at different temperatures. (c) CV curves of $LiMn_2O_4$ nanowall arrays synthesized at 240 °C at different scan rates. (d) Rate capabilities of $LiMn_2O_4$ nanowall arrays synthesized at different temperatures. (e) Cycle performance of $LiMn_2O_4$ nanowall arrays synthesized at different temperatures. (f) Schematic illustration of construction of flexible full cell device combining 3D $LiMn_2O_4$ cathode and 3D $Li_4Ti_5O_{12}$ anode. (g) Charge/discharge curves of the $LiMn_2O_4$ cathode, the $Li_4Ti_5O_{12}$ anode, and the $LiMn_2O_4$//$Li_4Ti_5O_{12}$ full cell. (h) Charge/discharge curves of the $LiMn_2O_4$//$Li_4Ti_5O_{12}$ full cell at different C rates. (i) Optical image of the flexible full cell device lighting a LED.

To investigate the electrochemical performance of the 3D $LiMn_2O_4$ electrode, half cells were first assembled using lithium anode and liquid electrolyte. Fig. 4a shows the first charge/discharge curves of the 3D $LiMn_2O_4$ cathodes prepared at different temperatures of 200, 220, and 240 °C (denoted as S1, S2, and S3) at 1 C rate. Sample S1 shows sloppy charge/discharge profile without obvious voltage plateaus, indicating low degree of crystallinity of $LiMn_2O_4$ synthesized at 200 °C. The initial discharge capacity of sample S1 is only about 100.6 mA h g^{-1}, which can be explained by its poor crystallization and existence of Mn_3O_4 impurity phase due to incomplete conversion as shown in XRD. As the synthesis temperature was increased to 220 °C, the charge/discharge curves demonstrate better defined voltage plateaus with a larger discharge capacity of about 120.2 mA h g^{-1}, attributing to its high phase purity and improved crystallization. Sample S3 prepared at 240 °C shows the highest discharge capacity of about 131.8 mA h g^{-1} with well-defined voltage plateaus, implying high degree of crystallinity and high electrochemical activity. The typical CV curves of the three samples at a scan rate of 0.1 mV s^{-1} between 3 and 4.4 V are compared in Fig. 4b. Agreeing well with the charge/discharge results, sample S3 with high degree of crystallinity displays two pairs of well-defined redox peaks between 3.9 and 4.2 V, which can be attributed to two phase transformations of $LiMn_2O_4/Li_{0.5}Mn_2O_4$ and $Li_{0.5}Mn_2O_4/MnO_2$ [40]. The redox peaks become weak and broad for the samples synthesized at lower temperatures, indicating low degree of crystallinity without an ideal spinel structure. In addition, the S3 sample shows the smallest potential difference between cathodic and anodic peaks, suggesting small polarization and low resistance of the electrode with high electrochemical activity. Fig. 4c shows the CV curves of the S3 sample at various scan rates from 0.1 to 10 mV s^{-1}. Even at the high scan rate of 10 mV s^{-1}, the CV curve of the S3 sample still retains well-defined redox peaks with only slight distortion, illustrating fast Li intercalation/deintercalation process and good rate capability. To compare the rate performance of each sample, the different electrodes were charged and discharged at different C rates and the specific capacities as a function of cycle number are shown in Fig. 4d. The S3 sample demonstrates much larger reversible capacities at different C rates compared to S1 and S2, exhibiting superior rate performance. The discharge capacities of the S3 sample are 131.8, 120.9, 110.4, and 97.1 mA h g^{-1} at 1 C, 5 C, 10 C, and 20 C, respectively, which outperform the rate performance of $LiCoO_2$/Al nanorod arrays [41], $LiCoO_2$ nanowire arrays [25], $LiMn_2O_4$/TiN/SiO_2 nanowire arrays [30], and C/$LiFePO_4$/Ti/Ni nanowire arrays [42]. The outstanding rate performance of the present $LiMn_2O_4$ nanowall arrays can be attributed to their small particle size, high level of crystallization, and porous structure, which facilitate fast Li^+ ion transport in the electrode. Besides the specific capacity and rate performance, the cycling performance of the electrode is also important for practical application of flexible lithium-ion batteries. Fig. 4e portraits the cycle performance of S1, S2, and S3 cycled at 1 C rate for 200 cycles at room temperature. The S3 sample shows the best cycling stability with 96% capacity retention after 200 cycles, which is much better than those of S1 (90%) and S2 (94%). The capacity fading of spinel $LiMn_2O_4$ is mainly attributed to structure degradation by volume variation during Li intercalation/deintercalation and Mn dissolution in the electrolyte. The samples with lower degree of crystallinity have a defective spinel structure with poor structural stability, which could accelerate structural degradation during cycling, thus leading to early capacity fading. The S3 sample, possessing well-defined spinel structure with high degree of crystallinity and mesoporous structure with small particle size, could well accommodate the volume changes and retain the structural integrity during repeated charging and discharging. More importantly, the 3D $LiMn_2O_4$ nanowall arrays (S3) exhibit a large areal capacity up to 0.29 mA h cm^{-2}, which is about 10 times larger than those of 2D planar $LiMn_2O_4$ thin film electrodes [43], and much larger than those of previously reported 3D thin film cathodes (Supporting Information, Table S1) [30,41,42]. Previously reported textured $LiMn_2O_4$ film [29] and 3D $LiMn_2O_4$ thin film [30] can only reach a maximum areal capacity of 0.01 ~ 0.03 mA h cm^{-2} due to the low active material loading (~0.15 mg) associated with their complicated synthesis procedures. The large areal capacity of the present $LiMn_2O_4$ nanowall arrays can be attributed to their large mass loading per area and 3D porous structure, which could effectively boost the energy density within a limited footprint area for microbatteries.

The cycle performance and rate performance between $LiMn_2O_4$ nanowall arrays and bulk $LiMn_2O_4$ powders were further compared to highlight the advantages of the unique $LiMn_2O_4$ nanowall arrays. For bulk $LiMn_2O_4$ powders, we purchased the commercial products from Shenzhen Tianjiao Technology; the morphology and XRD results for the conventional $LiMn_2O_4$ powders are shown in Figs. S7 and S8 in Supporting Information. Both electrodes were cycled between 3 and 4.4 V at 1 C rate for 200 cycles at room temperature. As shown in Fig. S9 (Supporting information), the $LiMn_2O_4$ nanowall arrays exhibit enhanced capacity retention (96%) compared to that of the bulk $LiMn_2O_4$ powders (94%). Importantly, the $LiMn_2O_4$ nanowall arrays can deliver much larger reversible capacity (~130 mA h g^{-1}) than that of the bulk $LiMn_2O_4$ powders (~110 mA h g^{-1}) at 1 C. The advantage of $LiMn_2O_4$ nanowall arrays was clearly proved by the rate performance comparison as shown in Fig. S10 (Supporting information). At 20 C rate, the $LiMn_2O_4$ nanowall arrays can still deliver a large reversible capacity of about 97 mA h g^{-1}, which is much greater than 46 mA h g^{-1} of bulk $LiMn_2O_4$ powders, demonstrating remarkably superior rate performance of the $LiMn_2O_4$ nanowall arrays. The outstanding electrochemical performance of the $LiMn_2O_4$ nanowall arrays can be attributed to their unique porous structure in following aspects: First, the high degree of crystallinity, small particle size, and mesoporous nanowall structure endow this electrode with greatly improved structural stability during cycling, thus leading to excellent cycling performance. Second, the porous structure and small particles' size can expedite electrolyte penetration into the electrode and enable fast ion diffusion with much shortened diffusion length, resulting in high utilization of the active material and outstanding rate performance.

The capacity fading of $LiMn_2O_4$ is mainly attributed to structural degradation caused by volume change and Mn dissolution during Li intercalation/deintercalation. The $LiMn_2O_4$ nanowall arrays possess mesoporous structure and small crystalline size, which could alleviate the stain associated with volume change and remain the structural integrity during repeated charge/discharge process, thus resulting in improved structural stability compared to conventional $LiMn_2O_4$ powders. When the testing temperature increases to 50 °C, it is clear that both $LiMn_2O_4$ nanowall arrays and conventional $LiMn_2O_4$ powders show deterioration in cycle performance, which is due to the aggravated Mn dissolution at elevated temperature (Fig. S11, Supporting information). Although the $LiMn_2O_4$ nanowall arrays should possess larger surface area compared to conventional $LiMn_2O_4$ powders, the cycle performance of the $LiMn_2O_4$ nanowall arrays is still superior to that of the conventional $LiMn_2O_4$ powders at elevated temperature, suggesting $LiMn_2O_4$ nanowall arrays might have stabilized surface that suppresses Mn dissolution in addition to the enhanced structural stability.

The 240 °C prepared $LiMn_2O_4$ nanowall arrays exhibit promising electrochemical performance, suggesting its high potential application in 3D microbatteries and flexible lithium-ion batteries. In this work, the $LiMn_2O_4$ nanowall arrays grown on carbon cloth were used as the cathode for flexible lithium-ion batteries. To construct the full cell, $Li_4Ti_5O_{12}$ nanowall arrays grown on carbon

cloth with similar morphology were used as the anode (Supporting information, Fig. S12). The XRD results indicate phase pure $Li_4Ti_5O_{12}$ was synthesized by the hydrothermal method (Supporting information, Fig. S13). Fig. 4f exhibits the schematic illustration of the full cell device construction with $LiMn_2O_4$ cathode and Li_4TiO_2 anode. Fig. 4g shows the typical charge/discharge curves of the $LiMn_2O_4$//Li half cell, $Li_4Ti_5O_{12}$//Li half cell, and $LiMn_2O_4$//$Li_4Ti_5O_{12}$ full cell at 1 C. As expected from the operating voltages of $LiMn_2O_4$ ($\sim$ 4 V) and $Li_4Ti_5O_{12}$ ($\sim$ 1.5 V), this full cell combination produces a battery with an operating voltage of about 2.5 V. The initial charge and discharge capacities of the full cell are 149.1 and 124.8 mA h g^{-1}, respectively, between 1.6 and 3.0 V at 1 C rate. The reversible capacity of the full cell was measured to be 105.6 mA h g^{-1} after 100 cycles. Except for the initial dozens of cycles, the coulombic efficiency for the rest of cycles is close to 100%. In addition to the good cycle performance, the full cell exhibits excellent rate capability as shown in Fig. 4h. Even at a high rate of 20 C, the full cell still can deliver a reversible capacity of about 92.1 mA h g^{-1}, which is about 73% of the reversible capacity at 1 C (Supporting information, Fig. S14). The flexibility of the full cell device was further investigated by testing the charge/discharge behavior and cycling stability at various bending states (Supporting information, Figs. S15–17). It is demonstrated that the full cell device retains almost the same charge/discharge curves and constant charge/discharge capacities at various bending states and after repeated bending cycles, proving good flexibility of the full cell device. For demonstration purpose, the fully charged full cell device was used to light a 3 V, 10 mW light emitting diode (LED). The full cell can continuously power the LED under different bending states (Supporting information, Fig. S18), implying good flexibility and potential application in flexible electronics.

4. Conclusions

In summary, the development of 3D cathodes that consist of self-standing $LiMn_2O_4$ nanowall arrays on various substrates is presented in this work. The “hydrothermal lithiation” can directly convert tetragonal spinel Mn_3O_4 into cubic spinel $LiMn_2O_4$ without destroying the base nanoarchitecture. The 3D $LiMn_2O_4$ nanowall arrays, featuring mesoporous structure and highly crystallized nanoparticles, exhibit large specific capacity (131.8 mA h g^{-1} or 0.29 mA h cm^{-2}), outstanding cycling stability (96% capacity retention after 200 cycles), and excellent rate capability (97.1 mA h g^{-1} at 20 C), which make them promising at cathodes for developing 3D microbatteries and flexible lithium-ion batteries. For the first time, a flexible battery using 3D $LiMn_2O_4$ nanowall arrays on carbon cloth as cathode and 3D $Li_4Ti_5O_{12}$ nanowall arrays on carbon cloth as anode has been demonstrated by powering LED. The 3D cathode design and the effective low-temperature synthesis route will lead to new opportunities to develop high-performance microbatteries and flexible lithium-ion batteries.

Acknowledgments

This work was supported by National Natural Science Foundation of China (No. 51572129, U1407106), Natural Science Foundation of Jiangsu Province (No. BK20131349), QingLan Project of Jiangsu Province, A Project Funded by the Priority Academic Program Development of Jiangsu Higher Education Institutions (PAPD), the Fundamental Research Funds for the Central Universities (No. 30915011204). J. K. S and Y.S. M acknowledge the seed funding from the Sustainable Power and Energy Center at UC San Diego.

Appendix A. Supplementary material

Supplementary data associated with this article can be found in the online version at http://dx.doi.org/10.1016/j.nanoen.2016.01.022.

References

[1] J.F.M. Oudenhoven, L. Baggetto, P.H.L. Notten, Adv. Energy Mater. 1 (2011) 10–33.
[2] Y.H. Hu, X.L. Sun, J. Mater. Chem. A 2 (2014) 10712–10738.
[3] Y.N. Zhou, M.Z. Xue, Z.W. Fu, J. Power Sources 234 (2013) 310–332.
[4] H.G. Zhang, X.D. Yu, P.V. Braun, Nat. Nanotechnol. 6 (2011) 277–281.
[5] J.M. Haag, G. Pattanaik, M.F. Durstock, Adv. Mater. 25 (2013) 3238–3243.
[6] N. Cirigliano, G.Y. Sun, D. Membreno, P. Malati, C.J. Kim, B. Dunn, Energy Technol. 2 (2014) 362–369.
[7] K. Sun, T.S. Wei, B.Y. Ahn, J.Y. Seo, S.J. Dillon, J.A. Lewis, Adv. Mater. 25 (2013) 4539–4543.
[8] J. Ren, Y. Zhang, W.Y. Bai, X.L. Chen, Z.T. Zhang, X. Fang, W. Weng, Y.G. Wang, H. S. Peng, Angew. Chem. Int. Ed. 53 (2014) 7864–7869.
[9] H. Gwon, J. Hong, H. Kim, D.H. Seo, S. Jeon, K. Kang, Energy Environ. Sci. 7 (2014) 538–551.
[10] X.F. Wang, X.H. Lu, B. Liu, D. Chen, Y.X. Tong, G.Z. Shen, Adv. Mater. 26 (2014) 4763–4782.
[11] B. Liu, J. Zhang, X.F. Wang, G. Chen, D. Chen, C.W. Zhou, G.Z. Shen, Nano Lett. 12 (2012) 3005–3011.
[12] T.S. Arthur, D.J. Bates, N. Cirigliano, D.C. Johnson, P. Malati, J.M. Mosby, E. Perre, M.T. Rawls, A.L. Prieto, B. Dunn, MRS Bull. 36 (2011) 523–531.
[13] B.L. Ellis, P. Knauth, T. Djenizian, Adv. Mater. 26 (2014) 3368–3397.
[14] J. Jiang, Y.Y. Li, J.P. Liu, X.T. Huang, C., Z. Yuan, X.W. Lou, Adv. Mater. 24 (2012) 5166–5180.
[15] Z. Liu, J. Xu, D. Chen, G.Z. Shen, Chem. Soc. Rev. 44 (2015) 161–192.
[16] X.F. Wang, B. Liu, X.J. Hou, Q.F. Wang, W.W. Li, D. Chen, G.Z. Shen, Nano Res. 7 (2014) 1073–1082.
[17] M.S. Balogun, M.H. Yu, Y.C. Huang, C. Li, P.P. Fang, Y. Liu, X.H. Lu, Y.X. Tong, Nano Energy 11 (2015) 348–355.
[18] D.L. Chao, C.R. Zhu, X.H. Xia, J.L. Liu, X. Zhang, J. Wang, P. Liang, J.Y. Lin, H. Zhang, Z.S. Shen, H.J. Fan, Nano Lett. 15 (2015) 563–573.
[19] Y.H. Wang, Y.H. Wang, D.S. Jia, Z. Peng, Y.Y. Xia, G.F. Zheng, Nano Lett. 14 (2014) 1080–1084.
[20] Y.L. Wang, T.Y. Wang, P.M. Da, M. Xu, H. Wu, G.F. Zheng, Adv. Mater. 25 (2013) 5177–5195.
[21] X.H. Xia, Q.Q. Xiong, Y.Q. Zhang, J.P. Tu, C.F. Ng, H.J. Fan, Small 10 (2014) 2419–2428.
[22] C. Wang, L.X. Wu, H. Wang, W.H. Zuo, Y.Y. Li, J.P. Liu, Adv. Funct. Mater. 25 (2015) 3524–3533.
[23] J.S. Luo, X.H. Xia, Y.S. Luo, C. Guan, J.L. Liu, X.Y. Qi, C.F. Ng, T. Yu, H. Zhang, H. J. Fan, Adv. Energy. Mater. 3 (2013) 737–743.
[24] W. Xiong, Q.Y. Xia, H. Xia, Funct. Mater. Lett. 7 (2014) 1430003.
[25] H. Xia, Y.H. Wan, W. Assenmacher, W. Mader, G.L. Yuan, L. Lu, NPG Asia Mater. 6 (2014) e126.
[26] L.Q. Mai, X.C. Tian, X. Xu, L. Chang, L. Xu, Chem. Rev. 114 (2014) 11828–11862.
[27] W. Tang, Y.Y. Hou, F.X. Wang, L.L. Liu, Y.P. Wu, K. Zhu, NanoLett. 13 (2013) 2036–2040.
[28] F.Y. Cheng, H.B. Wang, Z.Q. Zhu, Y. Wang, T. Zhang, Z.L. Tao, J. Chen, Energy Environ. Sci. 4 (2011) 3668–3675.
[29] B.G. Park, S. Kim, I.D. Kim, Y.J. Park, J. Mater. Sci. 45 (2010) 3947–3953.
[30] M. Bettge, S.Y. Ryu, S. Maclaren, S. Burdin, I. Petrov, M.F. Yu, E. Sammann, D. P. Abraham, J. Power Sources 206 (2012) 288–294.
[31] H. Xia, J.W. Zhang, X.G. Li, Nanosci. Nanotechnol. Lett. 4 (2012) 559–563.
[32] L.F. Shen, B. Ding, P. Nie, G.Z. Cao, X.G. Zhang, Adv. Energy Mater. 3 (2013) 1484–1489.
[33] W. Xiao, H. Xia, L. Lu, J. Electrochem. Soc. 156 (2009) A627–A633.
[34] D.W. Liu, B.B. Garcia, Q.F. Zhang, Q. Guo, Y.H. Zhang, S. Sepehri, G.Z. Cao, Adv. Funct. Mater. 19 (2009) 1015–1023.
[35] T.T. Li, C.L. Guo, B. Sun, T. Li, Y.G. Li, L.F. Hou, Y.H. Wei, J. Mater. Chem. A 3 (2015) 7248–7254.
[36] H. Xia, Y.H. Wan, F. Yan, L. Lu, Mater. Chem. Phys. 143 (2014) 720–727.
[37] C.M. Julien, M. Massot, C. Poinsignon, Spectrochim. Acta A 60 (2004) 689–700.
[38] H. Xia, K.R. Ragavendran, J.P. Xie, L. Lu, J. Power Sources 212 (2012) 28–34.
[39] G.H. Waller, S.Y. Lai, B.H. Rainwater, M.L. Liu, J. Power Sources 251 (2014) 411–416.
[40] Y.L. Ding, J.A. Xie, G.S. Cao, T.J. Zhu, H.M. Yu, X.B. Zhao, Adv. Funct. Mater. 21 (2011) 348–355.
[41] M.M. Shaijumon, E. Perre, B. Daffos, P.L. Taberna, J.M. Tarascon, P. Simon, Adv. Mater. 22 (2010) 4978–4981.
[42] Y.H. Liu, W. Zhang, Y.J. Zhu, Y.T. Luo, Y.H. Xu, A. Brown, J.N. Culver, C. A. Lundgren, K. Xu, Y. Wang, C.S. Wang, Nano Lett. 13 (2013) 293–300.
[43] Z. Quan, S. Ohguchi, M. Kawase, H. Tanimura, N. Sonoyama, J. Power Source 244 (2013) 375–381.